AIAA AVIATION Forum
12-16 June 2023, San Diego, CA and Online
AIAA AVIATION 2023 Forum

10.2514/6.2023-4239

Velocity and Vorticity Fields of a High-Frequency Pulsed Supersonic Co-Axial Injector

John T. Solomon[1], Noah Hackworth[2], Rhys Lockyer[2], Uriah Philip[2]
Tuskegee University, Tuskegee, AL, 36088

Philip Kreth[3]
University of Tennessee Space Institute, Tullahoma, TN 37388

This paper presents the velocity and vorticity fields of a supersonic, pulsed co-flow injection system, measured using particle image velocimetry (PIV). The active injection system consists of an actuation air jet from a nozzle (1 mm ID, 1.5 mm OD) that provides large mean and fluctuating velocity profiles to the shear layers of a fluid stream injected through a 460 µm diameter annular space surrounding the nozzle. The injector assembly is designed to operate in three modes in the present study. In the first case, annular fluid was injected at 70 m/s without actuation and treated as baseline flow. In the second case, a steady under-expanded supersonic jet with an exit velocity of 350 m/s interacts with the injected annular fluid. In the last case, the actuation jet pulsing at 15.5 kHz introduces high-frequency streamwise vortices and shockwaves to the annular stream. PIV data indicate that steady and pulsed actuation significantly modifies the velocity and vorticity fields of annular flow. While steady actuation caused intensive shear and high vorticity streaks in the flow, the high-frequency vortex generated in pulsed actuation resulted in highly fluctuating velocity and vorticity fields that favor enhanced mixing between the annular stream and supersonic actuation jet. Quantitative data from this study confirm the potential of this injector system for flow mixing and control under extreme conditions.

I. Introduction

The efficient mixing of two fluid streams moving at supersonic speed is a challenging problem experienced in high-speed combustors. Effective and controlled mixing is critical for the safety, economy, and stable operations of such systems. A co-axial jet configuration is a simple and effective mixing enhancement method in which fluids flowing separately through the inner core and the annular space meet at the exit plane of the nozzle assembly. For example, in applications like a gas turbine or combustion chamber of a rocket engine, these fluids could be oxidizers, such as gaseous or liquid oxygen, and fuel in its liquid or gaseous phase. Effective and controlled mixing can lead to higher combustion efficacy, longer life, reduced combustor size, stable operations, and fewer emissions/pollutants. Although the mixing ultimately happens at the molecular level, active flow control techniques can tailor the flow dynamics at micro and macro scales in favor of rapid diffusion at the molecular level [1-3].

One of the challenges for mixing in such extreme flow conditions is the microscopic convective time scale (order of milliseconds) associated with high-speed flow systems. Such a small time scale demands robust flow control actuators to enhance microscale mixing at high speed and positively alter the macroscopic phenomena. The entrainment and vorticity dynamics resulting from the shear layer instability modification also play a significant role in the overall efficiency of the mixing process. Passive methods proposed for improved mixing in high-speed systems use flush-mounted or intrusive injectors to generate streamwise, counter-rotating vortices for rapid nearfield mixing of the incoming air and fuel [4-12]. Beyond the classical passive co-axial configuration, a few studies explore active schemes such as powered resonance tubes (PRT) or Hartmann-Sprenger tubes as an option to excite

---

[1] Associate Professor, Department of Mechanical Engineering, Senior Member AIAA

[2] Research Assistant

[3] Assistant Professor, Department of Mechanical, Aerospace, and Biomedical Engineering, UTSI, Senior Member AIAA

the shear layer at high frequency [13]. It is reported that such active jet modulation is promising for improving penetration and high-speed mixing compared to unmodulated jets [13]. However, the limited operational bandwidth and larger size restrict their implementation in practical systems.

With an aim to improve mixing at extreme flow speed conditions, an active nozzle assembly integrated with high-frequency actuators has been developed recently at Tuskegee University by Solomon et al. [14]. More details of the actuator design, development, and prior implementation for various high-speed flow control applications are available in [15-19]. In a recent study that quantifies mixing using a planar laser-induced fluorescence (PLIF) technique, Solomon et al. report that mixing has significantly increased between the annular fluid and the actuation jet when the nozzle system operates in a high-frequency pulsing actuation mode in comparison to a classical steady, co-axial actuation mode [22, 23]. The present study aims to explore this interesting phenomenon further and to understand the flow dynamics of the pulsed flowfield quantitatively using the PIV technique.

Fig. 1 shows a schematic of the active co-axial injector and three modes of operation. The injector assembly shown in Fig. 1*a,* which operates in pulsing mode, has four major components: 1) compressed air from a source nozzle that enters, 2) an actuator block, 3) from which a high-frequency pulsed jet flows out, and 4) and the fluid stream that is emitted co-axially through an annular space surrounding the actuation jet nozzle as indicated in Figure 1. Both fluids meet co-axially at the exit plane of the assembly. In pulsed mode, the instabilities of the injected co-flowing fluid can be tailored using the pulsed supersonic actuation jet operating at a frequency range of 1-60 kHz. More details of this co-axial injector system, its design, fabrication, and flow mixing characteristics are available in [22].

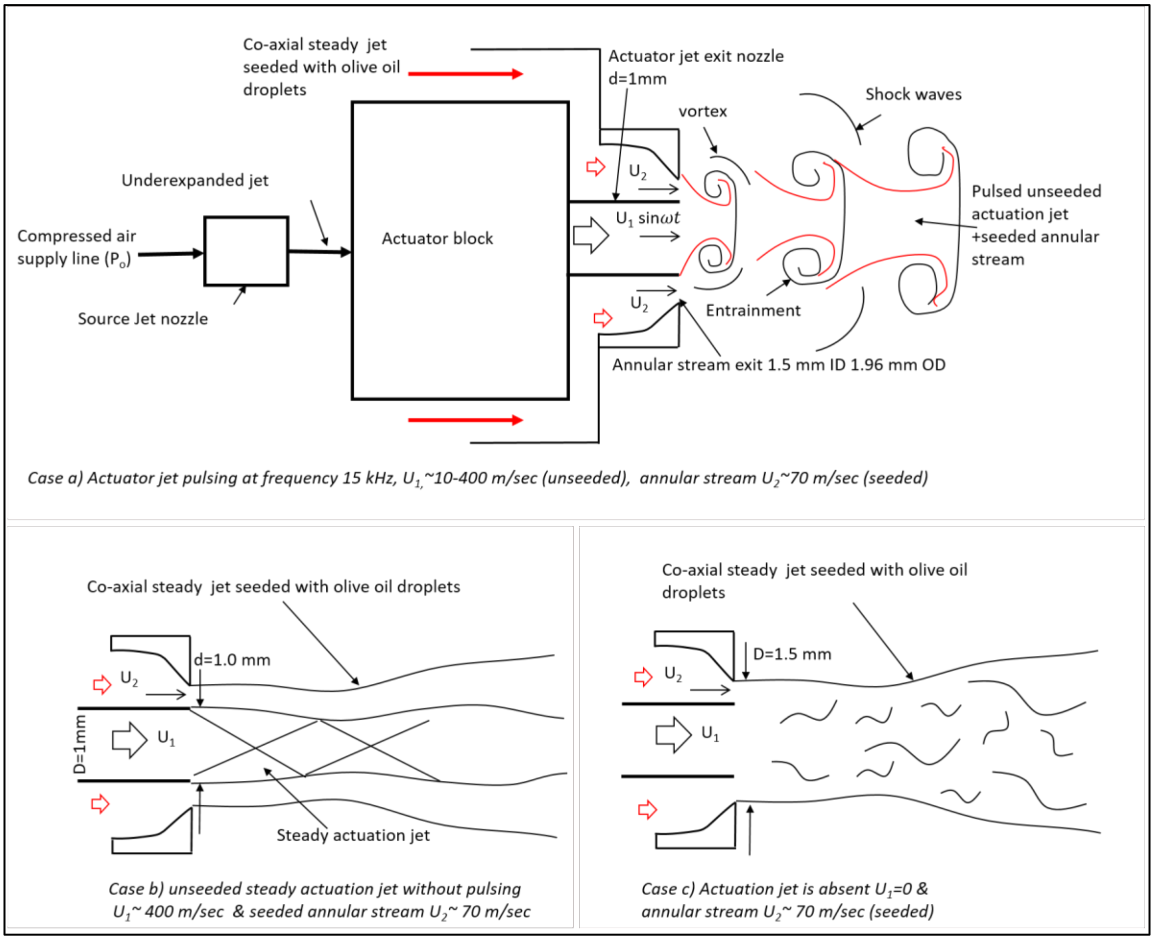

Case a) Actuator jet pulsing at frequency 15 kHz, $U_{1,}$~10-400 m/sec (unseeded), annular stream U_2~70 m/sec (seeded)

Case b) unseeded steady actuation jet without pulsing U_1~ 400 m/sec & seeded annular stream U_2~ 70 m/sec

Case c) Actuation jet is absent U_1=0 & annular stream U_2~ 70 m/sec (seeded)

Fig. 1 Schematic of the pulsed co-axial injector system and three operating modes *a)* Pulsed co-axial flow mode, *b)* steady co-axial flow mode, *c)* Annular flow without actuation jet

In the pulsed mode of operation, the inner actuation jet velocity U1 varies periodically from ~10-400 m/s at a design frequency of 15.5 kHz. This actuation jet provides highly unsteady velocity fluctuations to the annular flow at the exit, as indicated in Fig. 1*a*. The co-axial annular stream exits with a constant velocity of U2, depending on the injection pressure. For the present experiments, this velocity is set at 70 m/s. In the pulsed actuation mode of operation, the shear layer of the annular fluid is exposed to the ambient air on one side and the central pulsing jet's shear layer on the other. Fig. 1*b* shows a representative flow pattern of the flowfield at the exit when the nozzle assembly operates in a steady operation mode. The steady annular co-axial jet interacts with a supersonic, under-expanded actuation jet at the nozzle exit. Fig. 1*c* shows flow features when the injector operates in *no actuation* mode. Only the annular stream flows through the injector in this mode of operation.

Prior studies on this co-axial injector assembly using microschlieren and PLIF techniques confirm that the actuation jet exiting the nozzle assembly, surrounded by the annular fluid stream, generates high-frequency pulsed compressible vortices and shockwaves [18, 22]. The fluid injected through the outer annular core is entrained into the fast-moving compressible vortex and diffuses into it as it travels downstream. These vortexes and shockwaves excite the shear layer of annular flow on micro and macro scales, causing significantly enhanced mixing (up to 100%) between them [22]. The present study aims to understand this phenomenon and the flow dynamics of this actuator-integrated co-flow system through velocity and vorticity field measurements using PIV.

II. Experimental Details

A. Facility Description

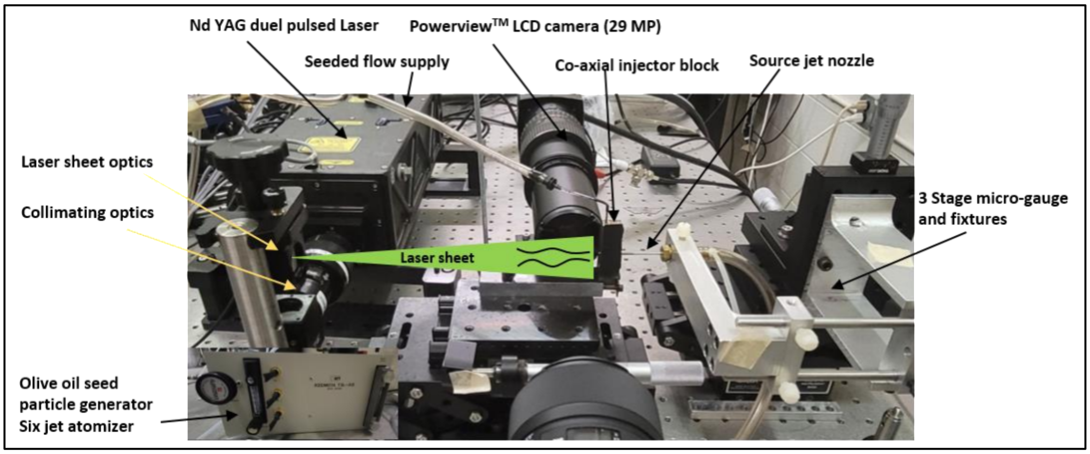

a) b)

Fig. 2 PIV set up established at Tuskegee University for the present study

a) Set up for particle image velocimetry (PIV)

The PIV imaging uses a setup, as shown in Fig. 2, established recently at Tuskegee University with support from the US National Science Foundation. The critical component of this setup is a Quantel EverGreen^{TM} Nd-YAG dual pulsed laser with a choice of pulse energies up to 200 *mJ* at 532 nm and 30 *mJ* at 266 nm with a repetition rate of 15 Hz. PIV experiments use laser low-energy level pulses at 532 *nm*. A Powerview^{TM} LS-LCD camera (29 MP, 6600x4400), with high quantum efficiency, low noise with 1.8 frames/s, selectable 12-bit or 14-bit output, and 100 mm f/2.8 camera lens, acquires the images. An eight-channel digital pulse synchronizer with 250 *ps* resolution controls the laser pulses and the trigger for the camera. A UV optic periscope and adjustable laser sheet optics (LSO) with 266/532 mm AR coat create a thin laser sheet at an appropriate test plane in the flowfield generated by the pulsed co-axial assembly. A six-jet oil droplet generator creates olive oil droplets in CO2 gas, forming the seeded annular fluid stream in the co-axial injector for velocity measurements. The image acquisition and analysis uses INSIGHT4G^{TM} software.

b) Measurement of nearfield spectra of actuator flowfield

The unsteady spectra of the flowfield of the active nozzle assembly were measured using a GRAS™ 1⁄4-inch Free-Field Microphone with a sensitivity of 4 *mV/Pa*. National Instruments™ 9234, 24-bit, 51.2 kHz data-acquisition module acquires the microphone data using LabVIEW™. Fast Fourier transformation (FFT) of time series with 2048 data points and Hann window with 50% overlap compute acoustic spectra used in the analysis. The source jet pressure measurement has an uncertainty of 0.1 psi. The micro-gauge used for linear movements of the nozzle block has an uncertainty of ±0.01 mm. A TSI^{TM} Mass Flow Multi-Meter 5300-4 measures the flow rate of CO2 with 2% reading accuracy for measurements up to 300L/min. A high-pressure compressed nitrogen tank (2000 psi) supplies air to the source jet nozzle and the pulsed jet injector assembly. A multi-channel oscilloscope monitors all signals used for measurements for accuracy.

B. Design details of the co-axial injector assembly

Figure 3 shows the design details of the pulsed co-axial injector assembly fabricated with three brass plates. The top plate contains a 3mm long, 1.3 mm diameter cavity through which an under-expanded actuator source jet enters the nozzle block. The second plate has another internal hole that forms the boundary for the resonance phenomena. 1 mm (ID) steel tube (with 1.5 mm OD) connects the cavity in the second plate and directs the air jet to flow out from the base of the third plate. The last plate has a 1.96 mm orifice, so when combined with the second plate and the steel tube with 1.5 mm OD, an annular space is formed outside the 1mm tube (ID). The internal cavity in plate 3 connects to a steady fluid (CO2) supply line through a steel tube. The design ensures no interaction or coupling between the co-axial fluids before they reach the exit plane of the assembly.

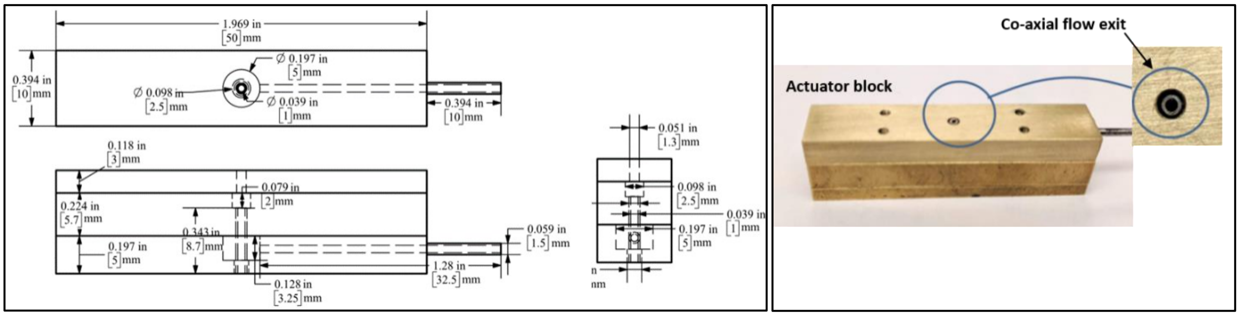

a) Front, top, and side view *b)Photograph of the injector*

Fig. 3 Design details of the co-axial injector a) front, side, and top views b) Photograph of the pulsed co-axial injector

This assembly has a total internal cavity volume of 20.6 mm$^{3.}$ The under-expanded source jet supplied from a nozzle of 1.5 mm exit diameter (*d*) enters the assembly through a 1.3 mm orifice located on the first plate. This source jet produces pulsed flow through the 1mm diameter tube integrated into the second and third plates under suitable resonance conditions. Such a design allows fluid stream (CO2) injection through the annular space while the central tube delivers a pulsed actuation air jet (N2) at a designed high frequency of 15.5 kHz. Experiments use two control parameters, *h/d* or nozzle pressure ratio, *NPR,* where *h* is the distance of the exit point of the source jet to the actuator cavity, and *d* is the source nozzle diameter, for frequency control. The present study uses *h/d* =1.3 and NPR=5.8 to achieve a pulsing frequency of 15.5 kHz.

C. PIV Data acquisition and processing methods

The PIV image acquisition and analysis used INSIGHT4G^{TM} software. A six-jet oil droplet generator creates fine olive oil droplets for seeding in CO2 gas, which is used as the annular fluid stream for velocity measurements. Figure 4 shows representative instantaneous raw images of the flowfield with oil seed particles at three different modes of operation as described earlier in Fig. 1. Figure 4*a* corresponds to a seeded annular jet at an exit velocity of 70 m/s without a co-flowing actuation jet at the center. Figure 4*b* shows the annular seeded jet actuated with a steady actuation jet from a source nozzle maintained at 65 psi pressure. At this pressure, the actuation jet velocity at the exit is sonic (~350 m/s). The actuation jet expands to supersonic speed (~400 m/s) outside the co-axial assembly as an under-expanded jet. Figures 4*c&d* are two instantaneous phases of the annular seeded jet actuated with a high-frequency actuation jet operating at 15.5 kHz from the same source maintained at 65 psi. Adjusting the parameter *h/d*, the actuation mode can be switched from steady to pulsing at the *same input pressure*. The annular nozzle is 1.96 mm in diameter, and the actuation jet exits from a nozzle of 1mm ID with 1.5 mm OD, which gives an annular exit dimension of 1.5mm diameter and 460-micrometer thickness as indicated in Fig. 4. The image calibration provides a resolution of 23 *µm/pixel* for the PIV data processing.

The field of view for PIV measurement is 20 mm across the flow and 50 mm in the streamwise direction. The major challenges for image acquisition are the flow scale (order of mm) and the higher speed of the co-axial stream resulting from the high-frequency supersonic jet actuation. The actuation jet in steady mode operates at a supersonic speed of 400+ m/s. The pulsing actuation provides a velocity fluctuation of ~10-400 m/s to the particle-seeded annular flow. The image acquisition parameters, such as time between the laser pulse (Δt), laser pulse delay, and PIV exposure time, were fine-tuned considerably to achieve image pairs with sufficient particle movements in various operating conditions. For the steady and unsteady actuation cases, the Δt is chosen at 0.40 microseconds, which will give 157 micrometers (μm) movement of seed particles at a velocity of 350 m/s.

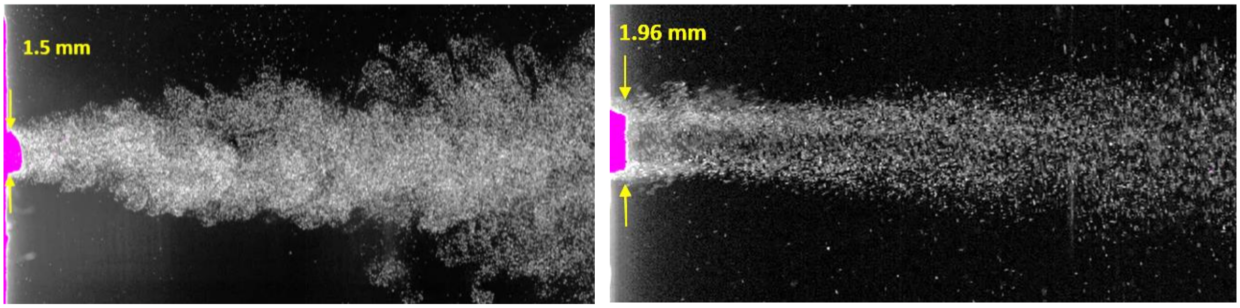

Particle seeded annular jet a) without actuation jet b) With steady actuation jet

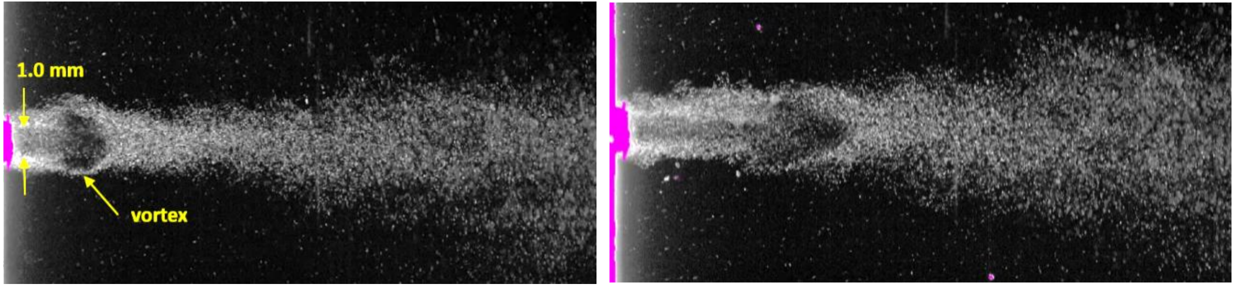

c) With pulsed actuation jet phase 1 d) With pulsed actuation jet phase 2

Fig. 4 Representative instantaneous raw images of the flowfield with oil seed particles at three different modes of operation

Since the image resolution is 23 μm/pixel, the seed particle will move at least 6-8 pixels distance at this measurement speed. The Δt is chosen at a higher value of 2 μs for measuring the low-velocity field of the annular flow moving at 70 m/s near the injector exit. The laser pulse repetition rate was kept at 1.5 Hz for all measurements. Since the Δt of the laser is extremely short at 400 nanoseconds, and the camera shutters have to close and adjust with the signals physically, there exists an actual delay in the timing for the camera exposure as opposed to the observation in the timing diagram shown in Fig. 5. The laser pulse delay time is fine-tuned to keep the two camera exposures in sync with the double laser pulses with the extremely short Δt.

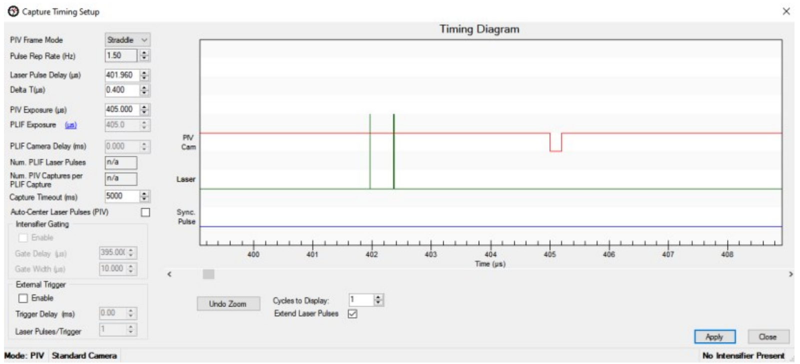

PIV Frame Mode: Straddle
Pulse Rep Rate (Hz): 1.50
Laser Pulse Delay (µs): 401.960
Delta T(µs): 0.400
PIV Exposure (µs): 405.000
PLIF Exposure (µs): 405.0
PLIF Camera Delay (ms): 0.000
Num. PLIF Laser Pulses: n/a
Num. PIV Captures per PLIF Capture: n/a
Capture Timeout (ms): 5000
Auto-Center Laser Pulses (PIV) ☐
Intensifier Gating
☐ Enable
Gate Delay (µs): 395.00(
Gate Width (µs): 10.000
External Trigger
☐ Enable
Trigger Delay (ms): 0.00
Laser Pulses/Trigger: 1
Cycles to Display: 1
Extend Laser Pulses ☑
Mode: PIV Standard Camera
No Intensifier Present

Fig. 5 Screen shot of timing diagram used for image acquisition

For 2D spatial calibration, a measured distance in the image –the outer tube diameter is 1.5 mm, measured within the image and used for calibration. A background removal technique generates cleaner and continuous vector fields during preprocessing. This technique uses the *Image Generator* plugin to calculate the minimum pixel intensity of the input images. This minimum intensity is subtracted from the raw images by the *Image Calculator*, which sets its operation parameter to *subtraction* and its operand parameter to the *image* and passes in the *generator image*. An appropriate processing mask is used for processing data in a region of interest 19 pixels from the nozzle.

The classic PIV processing algorithm is used for processing the images. Considering the intensive vorticity in the actuated flows, an additional PIV plugin, *Use Image Deformation*, which accounts for image deformation, has been used in the image processing approach for the highest accuracy. This plugin fixes the grid engine to *Deformation Grid* and the spot mask engine to *Deformation Mask*. The accuracy comes from the *Deformation Grid*, which performs subpixel deformation of particles across frames A and B. The *Deformation Mask* uses this subpixel deformation performance to condition and modifies the spots. The deformation grid settings were set values of 3 and 2 for the primary and secondary iterations. The interrogation window is selected from an initial size of 48x48 to a final dimension of 24x24. Having these differing spot dimensions between final and starting spot sizes increases the grid resolution by shortening the spatial area of one grid square, which occurs due to a determining factor. This allows the processor to draw more vectors as more interrogation spots are available. For a *Recursive Nyquist Grid*, a *final spot size* smaller than the *starting spot size* increases vector rows and columns by a factor of 2, which results in 4 times the number of vectors drawn with each pass. A similar effect is seen with the Deformation Grid plugin.

The correlation engine was set to *DirectCorrelator* to determine the particle movement between frames A and B by calculating and subtracting the mean intensity of spots, then summing the product of pixel intensities at each pixel offset. To further increase the accuracy of the *DirectCorrelator,* the engine adjusts the correlation map by an autocorrelation factor. The size of this map is limited by the maximum displacement value, which is a parameter that limits the maximum allowed displacement of a particle based on the ratio between *starting spot A* and *starting spot B* sizes, which is 1 in this case. This variable is important to limit bad/random vectors because extreme vectors can be filtered out by limiting how much a particle can be displaced. But in areas where particle displacement is too low, missing sectors in the vector field can occur, which are sections of the grid where vectors are absent. Therefore we set the maximum displacement value for the low velocity co-axial annular flow to 0.35 because of its low speed, causing lower overall particle displacement. For processing the annular flow without supersonic actuation, extreme vectors aren't something to worry about, so a value of 0.35 allows for more vectors of different magnitudes to be drawn. To process the vector field of annular flow with supersonic, steady, and pulse actuation, the maximum displacement value was set to 0.15 because extreme vectors are very likely in these flow types. Hence, 0.15 ensures a tight restriction that allows for a cleaner image. The *Gaussian Peak* algorithm was chosen for the peak engine to locate the displacement peak defined by the correlation engine. It locates the *peak* with subpixel accuracy by fitting a Gaussian curve to the highest pixel and its four nearest neighbors. We get our located peak from the application of two 3-point fits, one fit is done in the 'x' direction with the peak pixel and neighbors to the left or right of it, and one fit is done in the 'y' direction with the peak pixel and neighbors above and below it. The *GaussianPeak* and *DirectCorrelator* were used for the image pair analysis for the vector field prediction.

Within the processing plugin, *Double Correlation* was enabled to validate vectors and clean the vector field before post-processing. It validates vectors by taking the ratio between two correlation maps and measuring that ratio against the tolerance value, which was set to 3.5. One of the two correlation maps is the correlation map of the central vector in a square area; the other correlation map is the product correlation map acquired from multiplying the correlation maps of every vector surrounding that central vector. Any ratio above 3.5 invalidates that central vector, whereas any below 3.5 doesn't. The default tolerance value is 2, so a value of 3.5 was used so that there was some leeway given to the vectors while still maintaining some restriction to reduce bad/erroneous vectors. It's important to note that too tight of a restriction will label vectors of higher magnitudes invalid. So while the vector field may look good and represent flow behavior, further analysis will show a flow that's not within the velocity range it's supposed to be (i.e., supersonic actuation may appear to not be in the sonic or supersonic range). Within the processing, three secondary peaks were also exported; these will be used later in post-processing.

The post-processing for all flow types uses a *Global Validation*, a *Local Validation*, and a Vector *Field Conditioning* plugin to clean up the vector field. The 'Local Validation' comes before the 'Vector Field Conditioning' by convention but is recommended so that holes in the field can be better filled once the vectors are determined to be good or not. The *Global Validation* plugin was set to the 'standard deviation' range type, with a standard deviation factor of 4.5. Across the whole vector field, this plugin will determine what constitutes a valid vector by detecting invalid vectors that don't meet the requirements of the standard deviation factor. The factor determines the range of valid velocities from a central point valued at the mean velocity. For a vector to be considered valid, it is required that its velocity falls within this range, and a factor of 4.5 produces some room for vectors to be considered good but still applies a tight restriction so that errant vectors won't be considered good. This plugin is suitable for removing completely erroneous data. Using the Mean Test, the Local Validation plugin was used to validate vectors in a neighborhood of 5x5. The tolerance was set to 2.5 in both the U and V directions. When the *local validation* operates, it calculates a reference vector based on the mean of a 5x5 neighborhood, using each vector in that neighborhood; the reference vector is then compared to the current vector of the neighborhood. The difference between the current and reference vector is compared to the tolerance, and if the difference is less than the tolerance, the current vector is good, and if it's higher, then the current vector is bad. The default tolerance was 2, but the tolerance was changed to 2.5 to give a little extra leeway to some vectors but still keep a tight restriction. A difference higher than the tolerance means that the current vector drawn during processing is much higher than it should be, and 2.5 ensures that those types of vectors are invalidated. In this plugin, *By Valid Secondary Peak,* and *By Local Median* were enabled to replace those bad vectors. *By Valid Secondary Peak* uses the three secondary peaks exported during processing for replacement, and *By Local Median* uses the local median of the 5x5 neighborhood. Both replacement methods are enabled to increase the replacement rate of bad vectors.

The *Vector Field Conditioning plugin* will fill any holes resulting from failed vector validation. The plugin was set to recursively fill the holes of a 7x7 neighborhood using the mean vector of that local area as the filler vector. The *Recursive Filling* will do repeated passes of filling, first using the most valid neighbors for replacement vectors; then the second pass uses the second most valid neighbors; valid neighbors can be both measured and interpolated vectors. In this plugin, smoothing was enabled, with a *Gaussian Kernel* of 1 in a 5x5 neighborhood. Enabling this parameter adds a low-pass filter to the vector field after filling holes, tilting vectors towards their intended horizontal or vertical direction. This reduces some of the noise caused by random particle displacements. This process ultimately produces a clean but interpolated vector field.

III Results and Discussions

A) Frequency characterization of the pulsed co-axial assembly

Figure 6 shows the frequency spectra of the actuator integrated into the nozzle assembly measured using a GRAS™ microphone that picks acoustic signals from the near field. The pulsed co-axial flow shows a distinct frequency at 15.5 kHz, while the steady co-axial injection shows no specific tones in the spectra other than broadband noise. In steady actuation, energy is in broadband and is focused at 15.5 kHz for pulsed actuation. The spectra of the seed jet show low amplitude broadband noise indicating natural instabilities in the flow.

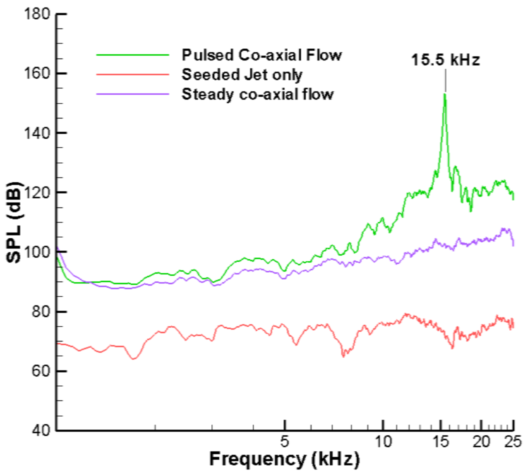

Fig. 6 spectra of actuator at three modes operation-pulsed, steady and no actuation

B) Instantaneous velocity and vorticity fields

a) Subsonic seeded annular flow without co-axial actuation jet

The present experiments use pressure and the flow rate of CO2 (annular stream) at 8 psi and 4.7 lit/min, respectively. For a given annular exit area of 1.08 mm^2, this flow rate gives an estimated exit velocity of U2 ~70 m/s for the seeded CO2 jet. The exit velocity U1 of the pulsed jet varies from 10-400 m/s during the cycle giving rise to a range for velocity ratio U1/U2~0-6. The exit flow area ratio *A1/A2* of the present configuration is 0.72, where A1 is the area exit of actuator flow, and A2 is the area of the annular space. With a pressure ratio of fluids exiting the assembly (P_{act}/P_{stream}) that varies in the range of 1- 13 during the pulsed co-axial injection process, the momentum of the actuation jet dominates the flowfield for the most part of the pulsing cycle.

Figure 7*a&b* shows a representative instantaneous velocity field of the seeded annular flow without a co-axial actuation jet. The annular stream from the nozzle merges to form a continuous jet with a maximum stream velocity measured up to 70 *m/s.* The merged jet core of the annular stream is visible up to 15 mm from the exit. The stream slowly dissipates into the ambient air, and the velocity drops to 10-20 m/s at 30 mm from the injector exit. The velocity field captures the natural instabilities present in the shear layer of the annular flow.

Figures 8a&*b* indicate the vorticity field of the injector corresponding to velocity vectors shown in Figure 7. The top and bottom annular flow regions form a vorticity core with a maximum magnitude of ±50000/s. Beyond this length, the vorticity core disintegrates and dissipates to a lower magnitude. Since the annular stream experience shear on both the inner and outer sides of the stream, four distinct dissipated vorticity streaks are observed in the axial direction in the images in Fig. 8.

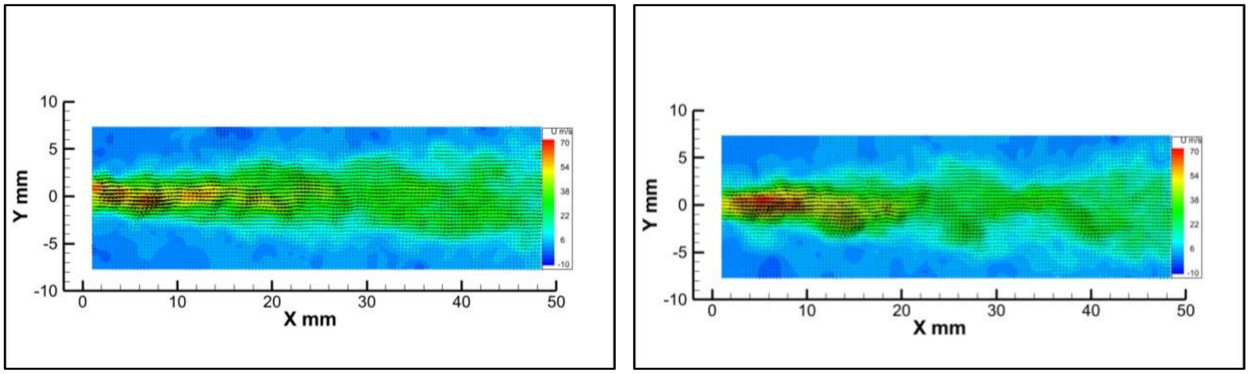

a) b)

Fig. 7 Instantaneous velocity fields of the seeded annular jet without actuation

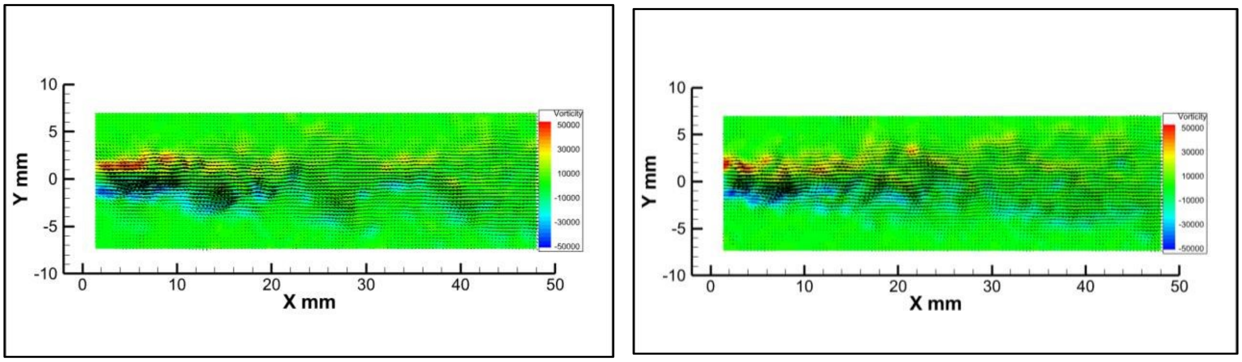

a) b)

Fig. 8 Instantaneous vorticity fields of the seeded annular jet correspond to Fig. 7

b) Subsonic seeded annular flow with supersonic steady co-axial actuation

Figure 9 shows representative instantaneous velocity fields of the seeded annular flow with steady jet actuation at the center. The steady actuation jet is an underexpanded jet supplied at a pressure of 65 psi, providing a sonic velocity (350 m/sec) at the exit of the injector. The unseeded supersonic actuation jet accelerates and entrains the seeded oil particles of the annular flow as it moves downstream. As observed in Fig. 9*a*, the entrainment is minimal near the nozzle exit. The highly underexpanded characteristic of the actuation jet and the strong compressible shear layer restricts diffusion of the seeded annular stream near the nozzle exit.

Due to steady jet actuation, the seed particles in the annular stream attain a maximum speed of 400 m/s at the core after moving through a distance of 5 to 20 mm from the nozzle exit. The overall velocity of the annular stream is increased significantly due to the high-momentum steady actuation jet. Figure 10 shows the corresponding two instantaneous vorticity fields of the seeded annular jet actuated with the steady under-expanded jet. As expected, the actuation causes continuous and intensive double vorticity streaks in the annular stream in the streamwise direction. The high vorticity magnitude (200,000/s) indicates that the actuation jet imparts intensive shear to the annular stream at the core. The magnitude of maximum vorticity has increased 4 times due to the steady jet actuation at the center core of the annular stream. The continuous vorticity streaks have extended up to 20 mm in the streamwise direction. The quantitative effects of steady actuation are evident from the velocity and vorticity fields shown in Figures 9 and 10. It significantly increased the velocity and vorticity of the annular fluid in the streamwise direction.

c) Subsonic seeded annular flow with supersonic pulsed co-axial actuation at 15.5 kHz

Figures 11 & 12 show four instantaneous velocity fields of a co-axial seeded annular stream when the actuation jet pulses at 15.5 kHz. These velocity fields correspond to four phases of the pulsed actuation. For example, Fig. 11*a* represents the instantaneous velocity field at the beginning phase (0^o)of the pulsed actuation observed with an evolving vortex near the nozzle. This vortex evolves, grows, and moves downstream in the streamwise direction in phase 90^o, as observed in Fig. 11*b*.

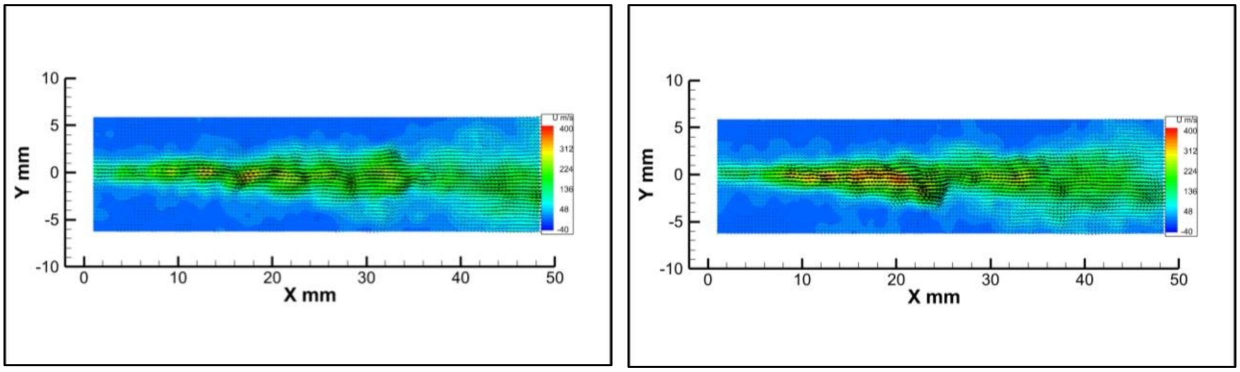

a) b)

Fig. 9 Instantaneous velocity fields of the seeded annular jet with steady actuation jet

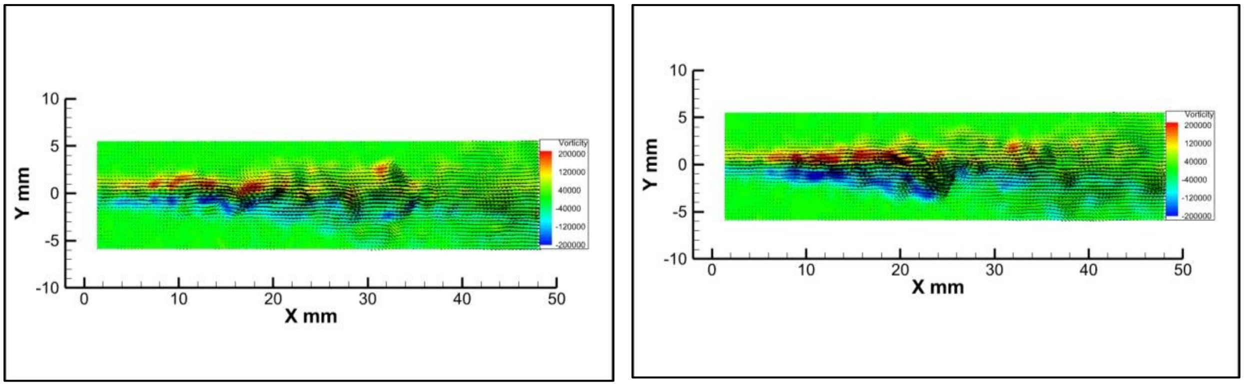

a) b)

Fig. 10 Instantaneous vorticity fields of the seeded annular jet with steady actuation jet

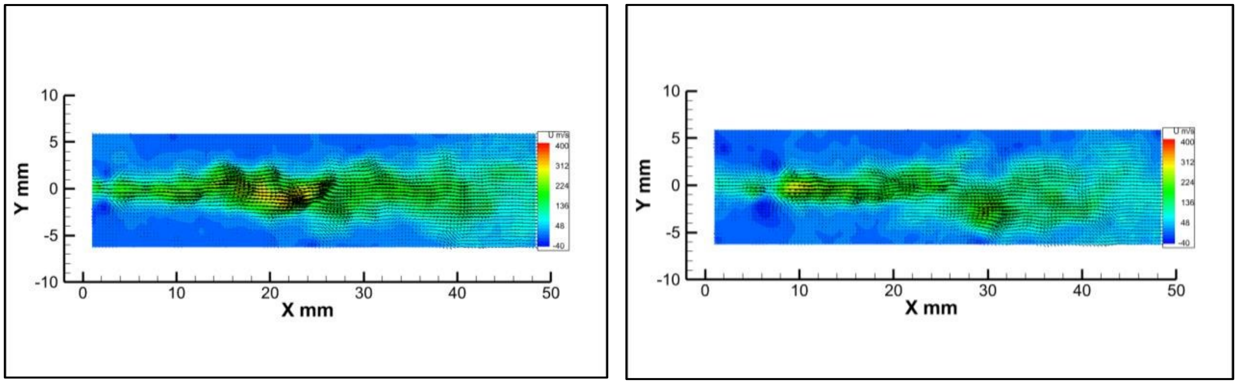

a) 0^o Phase b) 90^o phase

Fig. 11 Instantaneous velocity fields of the seeded annular jet with pulsed actuation jet operating at 15 kHz

As evident in phase 180°, as shown in Fig. 12, the growth and entrainment of annular fluid increase as it moves further downstream. At phase 270° pulsed vortex weakens considerably with interaction with the annular fluid and the air in the ambiance. The representative velocity fields of pulsed actuation at various phases of actuator operation confirm that the active injection offers significant velocity fluctuations in the mean flow of annular fluid. For example, in comparison of instantaneous images at phases 90° and 180° reveals, velocity fluctuations in a range of ~100-400 m/s in the streamwise location 10-20 mm from the nozzle exit.

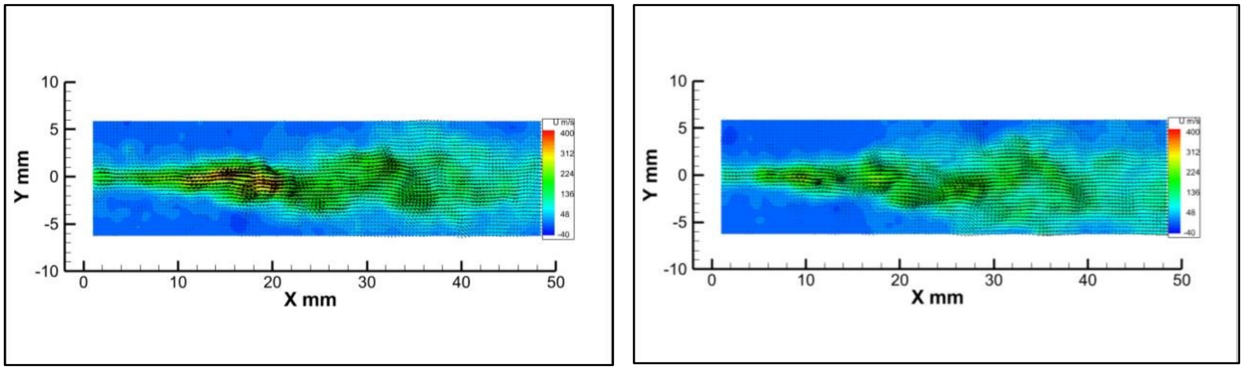

a)180° Phase b)270° Phase

Fig. 12 Instantaneous velocity fields of the seeded annular jet with pulsed actuation jet operating at 15 kHz

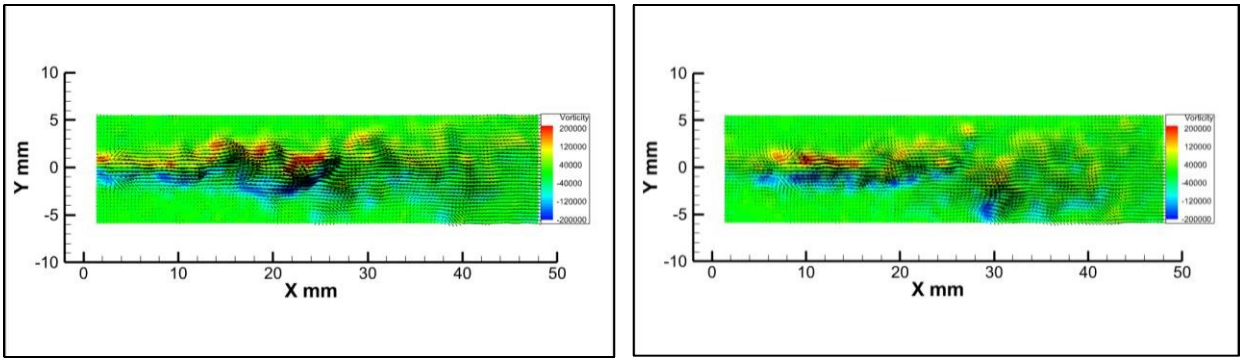

a) 0° Phase b) 90° phase

Fig. 13 Instantaneous vorticity fields of the seeded annular jet with pulsed actuation jet operating at 15 kHz

Figures 13 and 14 show four instantaneous phases of vorticity fields corresponding to the velocity fields in Figures 11 and 12. The evolving vortex, its growth, and its movement downstream in the streamwise direction are captured in these images. As evident in phase 180°' shown in Fig. 14, the growth and entrainment of annular fluid increase as it moves further downstream.

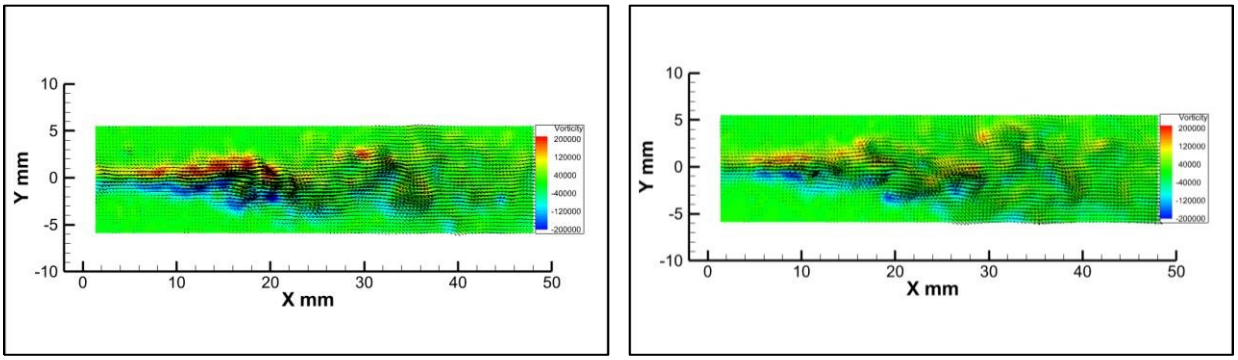

a) 180° Phase b) 270° phase

Fig. 14 Instantaneous vorticity fields of the seeded annular jet with pulsed actuation jet operating at 15 kHz

At phase 270° pulsed vortex weakens considerably with interaction with the annular fluid and the air in the ambiance. Such a highly unsteady vorticity field leads to enhanced mixing between the annular fluid and the high-velocity actuation jet. The maximum magnitude of the vorticity is observed to be the same in both steady and pulsed actuation cases.

Figures 15-17 show averaged velocity and vorticity fields of 260 images of three cases *a-c* discussed –annular fluid without actuation, with steady, and pulsed actuation, respectively. Due to the steady actuation, the core of annular fluid velocity and vorticity fields extended significantly from the nozzle exit in the streamwise direction. The maximum value of vorticity magnitude increases to 400% due to steady jet actuation and the velocity from 70 to 300 m/s.

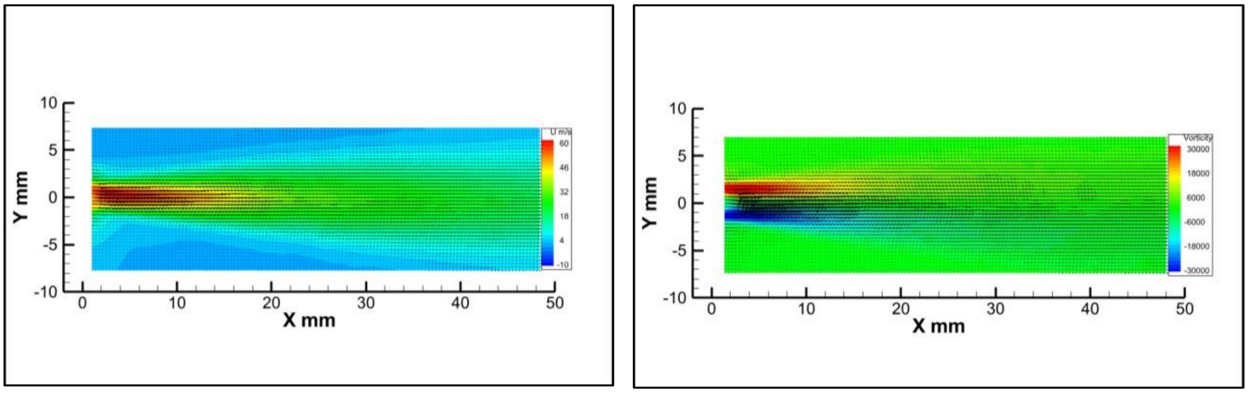

a) Average velocity field b) Average vorticity field

Fig. 15 Average velocity and vorticity fields of the seeded annular jet without actuation

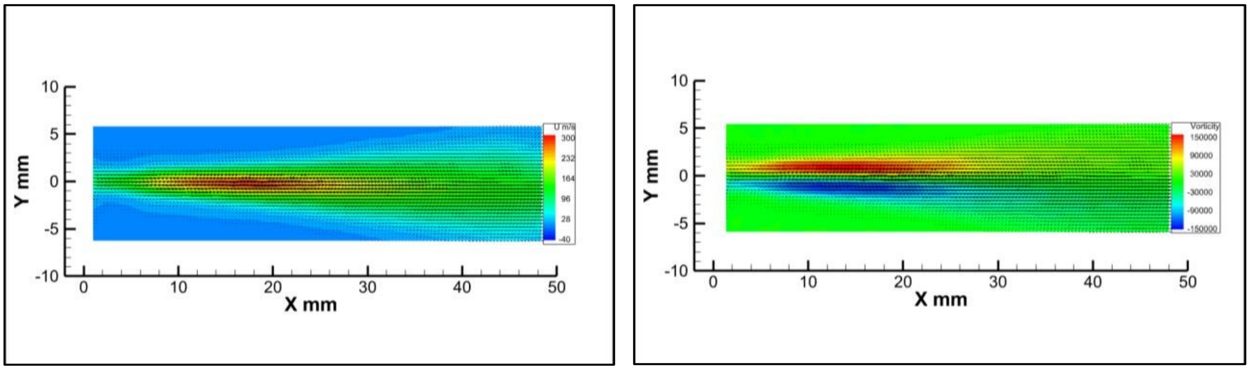

a) Average velocity field b) Average vorticity field

Fig. 16 Average velocity and vorticity fields of the seeded annular jet with steady jet actuation

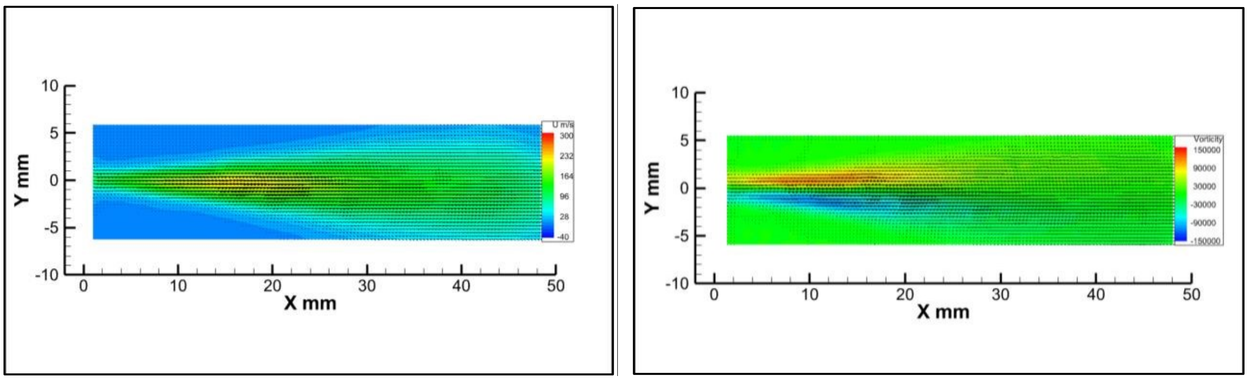

b) Average velocity field b) Average vorticity field

Fig. 17 Average velocity and vorticity fields of the seeded annular jet with pulsed jet actuation

A comparison of Fig 16*a* and 17*a* shows pulsed actuation leads to lower average velocity for annular stream than steady actuation. This observation is as expected due to the vortex formation in the pulsed flow. The average intensity of the vorticity field was also reduced in this case, as evident from Fig. 16*b* and 17*b*. The steady and pulsed actuation cases show two distinct patterns of annular stream diffusion. The high momentum steady actuation jet entrains the annular fluid to its core and increases speed to supersonic with less diffusion to ambient air. Its diffusion characteristics increase as the velocity decreases beyond 30 mm from the exit. For pulsed actuation, entrainment and diffusion begin at the nozzle exit and progress uniformly in the streamwise direction due to the evolving compressible vortex. This process leads to a more diverging flowfield and attributes enhanced mixing characteristics than steady actuation.

IV Summary

The paper reports an experimental study on an active, supersonic co-axial jet injection assembly integrated with ultra-high frequency pulsed microactuators. The assembly steadily injects a fluid through a 460µm annular space around a 1 mm ID, 1.5 mm OD sonic nozzle with an exit velocity of 70 m/s. The co-axial nozzle at the center (1 mm ID) issues the supersonic actuation jet in two operation modes: a) as steady under expanded jet at 65 psi and b) as pulsed actuation jet operating at 15.5 kHz at the same input pressure. The velocity and vorticity field of annular fluid with and without actuation were measured using particle image velocimetry (PIV). The steady actuation has increased the velocity up to 400 m/s and introduced four times intensive shear and extended vorticity streaks in the annular stream. The pulsed actuation resulted in fast-moving, high-frequency compressible air vortices in the injected flowfield. The growth and entrainment of these pulsed vortexes cause a highly unsteady velocity field and vorticity streaks in the annular stream. The current study confirms that the co-axial injector operating in pulsed mode can provide tailored vorticity in fast-moving fluids and be used for high-speed flow mixing and control applications.

Acknowledgments

National Science Foundation supports this work through grant 1900177.

References

1. B. Ritchie, D. Mujumdar, and J. Seitzman, "Mixing in co-axial jets using synthetic jet actuators," AIAA-2000-04-04.
2. Davis, S. A. & Glezer, A., "Mixing Control of Fuel Jets Using Synthetic Jet Technology: Velocity Field Measurements," AIAA Paper 99-0447.
3. Broadwell, J. E. and Mungal, M. G., "Large Scale Structures and Molecular Mixing," Physics Fluids, 1193-1206, 1991.
4. Kraus, D. K., and Cutler, A. D., "Mixing of Swirling Jets in a Supersonic Duct Flow," Journal of Propulsion and Power, Vol. 12, No. 1, 1995, pp. 170–177. doi:10.2514/3.24007
5. Cutler, A. D., and Doerner, S. E., "Effects of Swirl and Skew upon Supersonic Wall Jet in Crossflow," Journal of Propulsion and Power, Vol. 17, No. 6, 2001, pp. 1327–1332. doi:10.2514/2.5882
6. Drozda, T. G., Baurle, R. A., and Drummond, J. P., "Impact of Flight Enthalpy, Fuel Stimulant, and Chemical Reactions on the Mixing Characteristics of Several Injectors at Hypervelocity Flow Conditions," NASA Langley Research Center, May 2016, https://ntrs.nasa.gov/ archive/nasa/casi.ntrs.nasa.gov/20160009131.pdf [retrieved May 2017].
7. Gruber, M. R., Nejad, A. S., Chen, T. H., and Dutton, J. C., "Transverse Injection from Circular and Elliptic Nozzles into a Supersonic Crossflow," Journal of Propulsion and Power, Vol. 16, No. 3, 2000, pp. 449–457. doi:10.2514/2.5609
8. VanLerberghe, W. M., Santiago, J. G., Dutton, J. C., and Lucht, R. P., "Mixing of a Sonic Transverse Jet Injected into a Supersonic Flow," AIAA Journal, Vol. 38, No. 3, 2000, pp. 470–479. doi:10.2514/2.984
9. Shigeru, A., ArifNur, H., Shingo, M., Kei, I., and Yasuhiro, T., "Fundamental Study of Supersonic Combustion in Pure Air Flow with Use of Shock Tunnel," Acta Astronautica, Vol. 57, Nos. 2–8, 2005, pp. 384–389. doi:10.1016/j.actaastro.2005.03.055
10. Menon, S., "Shock Wave Induced Mixing Enhancement in Scramjet Combustors," AIAA Paper 1989-0104, 1989. doi:10.2514/6.1989-104 [
11. Ben-Yakar, B., Mungal, M. G., and Hanson, R. K., "Time Evolution and Mixing Characteristics of Hydrogen and Ethylene Supersonic Crossflow," Physics of Fluids, Vol. 18, No. 2, 2006, Paper 026101. doi:10.1063/1.2139684
12. Hsu, K., Carter, C. D., Gruber, M. R., and Tam, C., "Mixing Study of Strut Injectors in Supersonic Flows," AIAA Joint Propulsion Conference, AIAA Paper 2009-5226, 2009. doi:10.2514/6.2009-5226
13. Hongbin, G., Zhi, L., Fei, L., Lihong, C., Shenglong, G., and Xinyu, C., "Characteristics of Supersonic Combustion with Hartmann-Sprenger Tube Aided Fuel Injection," AIAA Conference, AIAA Paper 2011-2326, 2011. doi:10.2514/6.2011-2326

14. Solomon, J. T., Cairnes, K., Nayak, C., Jones, M. and Alexander, D. Design and Characterization of Nozzle Injection Assemblies Integrated High-frequency Microactuators. AIAA Journal Vol. 56, No. 9, pp. 3436-3448, 2018.
15. Ali MY, Arora N, Topolski M, Alvi FS, and Solomon JT. Properties of Resonance Enhanced Microjets in Supersonic Crossflow" AIAA Journal, AIAA Journal, Vol. 55, No. 3, pp. 1075-1081. https://doi.org/10.2514/1.J055082, 2017.
16. Uzun, A., Solomon, J.T., Foster, C.H., Oates, W.S., Hussaini, M.Y., Alvi, F.S. Flow physics of a pulsed microjet actuator for high-speed flow control. AIAA Journal Volume 51, No. 12, pp 2894-2918, 2013.
17. Solomon, J. T., Foster, C., and Alvi F.S. Design, and characterization of High-Bandwidth, Resonance Enhanced, Pulsed Microactuators: A parametric study. AIAA Journal, Volume 51, No. 2, pp 386-396. , 2013.
18. Solomon, J. T., Kumar, R., and Alvi, F.S. "High-Bandwidth Pulsed Microactuators for High-Speed Flow Control," AIAA Journal, Vol. 48, No. 10, pp. 2386-2396, doi.org/10.2514/1.J050405, 2010.
19. Solomon, J, T. High-bandwidth Unsteady Actuators for Active Control of High-Speed Flows," Ph.D. Dissertation, Florida State University. http://purl.flvc.org/fsu/fd/FSU_migr_etd-1642, 2010.
20. Lozano, A., Smith, S. H., Mungal, M. G. and Hanson, R. K., "Concentration Measurements in a Transverse Jet by Planar Laser-Induced Fluorescence of Acetone" AIAA Journal 32, 218-221, 1994.
21. Lozano, A., Yip, B., and Hanson, R. K., "Acetone: a by planar laser-induced fluorescence," Experiments in Fluids 13, 369-376, 1992
22. Solomon, J.T., Lockyer, R., Jones, T., Kreth, P., "High-Frequency Pulsed Co-axial Injectors for High-Speed Flow Mixing and Control," AIAA- 2022-3926
23. Solomon, J.T., Lockyer, R., Philip, U., Kreth, P., "Planar Laser-Induced Fluorescence (PLIF) Studies on a High-frequency Pulsed Co-Axial Injector Flowfield" FMFP-2022-9948, IIT Roorkee, India